

Exploration of Venus' Upper Atmosphere Using an Aqua and Bacteria Inspired Aerial System

Jackson Erb¹, Emily Strauss², Masoud Naghdi³, Mostafa Hassanalian⁴

This paper aims to design a jellyfish-inspired robot for the exploration of Venus' atmosphere. Venus' hostile environment necessitates different methods for planetary analysis than that of Mars or Earth. In this research, an established jellyfish-inspired drone design is modified to take advantage of Venus' dense atmosphere for the purpose of upper atmospheric exploration. The original design uses modified Stephenson-I 6-Bar linkages to actuate a soft skin to produce thrust in a fluid, similar to the movement of a jellyfish's bell; this research compares the original actuator design to 3 new designs based on the 6-Bar and 4-Bar linkages. In addition, a Crank mechanism to change the profile of the balloon is proposed, and the resulting effect on the drag force is compared between the original spherical profile and the modified oblong profile. These mechanisms will allow the robot to maximize its operational time in Venus's atmosphere. In combination with the design of the jellyfish-inspired robot is the proposal of flagellate-inspired robots that rely on Venus's strong winds to power its host of sensors.

I. Introduction

Since the 1960's, several countries such as the United States, Russia, Japan, and Europe have planned and executed missions to observe atmospheric, climate, and structural characteristics of Venus¹⁻³. The last dedicated mission to Venus was in 1989 with NASA's Magellan spacecraft that used a Synthetic Aperture Radar to map its surface¹. The spacecraft that had the longest duration of survival on the surface of Venus was the USSR's Venera 13 probe, which lasted for 127 minutes¹⁻³. The lander touched down on March 1, 1982, and took panoramic images of the Venusian surface, transmitting the first colored pictures. The lander also carried out scientific studies related to Venus' atmosphere and soil composition.

Due to its similar size, complex atmosphere, and surface composition, Venus is commonly known as Earth's twin⁴. However, Venus is not as welcoming with overwhelming temperatures (over 800°F), thick atmosphere, corrosive and high-pressure environments. At the surface, temperatures of almost 900°F are recorded, which is hot enough for conventional electronic systems to overheat⁴⁻⁶.

Many projects issued by NASA and other space agencies have investigated the feasibility of a purely mechanical-based rover to perform scientific analyses on the hot planet's surface. One example is the Automaton Rover for Extreme Environments (AREE), which uses gears, springs, and other mechanical components to provide rover mobility, power generation, and functionality without having the worry of electronic overheating⁷. Other projects, such as aerial platforms, have also been explored to investigate the Venus environment and avoid the harsh conditions of the surface, looking at the atmospheric circulation and chemical nature⁸⁻¹⁰.

¹ Undergraduate Student, Department of Mechanical Engineering, Clemson University, Clemson, SC 29631, USA.

² Undergraduate NSF REU Student, Department of Mechanical Engineering, New Mexico Tech, Socorro, NM 87801, USA.

³ PhD, visiting Scholar, Department of Mechanical Engineering, New Mexico Tech, Socorro, NM 87801, USA

⁴ Assistant Professor, Department of Mechanical Engineering, New Mexico Tech, Socorro, NM 87801, USA

There is an interest in the aerospace and scientific community for developing new concepts and methodologies with energy harvesting techniques that can broaden the scope and range of Venusian scientific discoveries¹¹⁻¹⁶. This work discusses a new concept involving a hybrid aerial system inspired by a jellyfish and bacteria-based organism – Flagellates – that travel along and draws power from the strong winds in the upper atmosphere of Venus (see Figures 1 and 14). The jellyfish-inspired robot is designed to carry these flagellate drones while remaining neutrally or positively buoyant in Venus' atmosphere, while the flagellate systems are equipped with various sensors needed for climate monitoring, topographical mapping, chemical composition and much more. This concept can provide an answer about Venus' atmospheric development, evolution, and climate history. In addition, it has significant merit for Earthbound applications such as aquatic underwater sensing, medical screenings, sensor imagery, and other aviation and aerospace missions

II. Design of Jellyfish Robot

A. Conceptual Design Overview

The mechanical design of the robot is composed of two distinct modules: the bell actuator mechanism and the inflatable balloon. The actuators that have been developed based on a previous study are designed, when attached to a flexible skirt, to mimic the movements of a jellyfish's bell and eject water to produce movement¹⁷. Both the original design and the concept developed in this research are presented in Figure 1. The movement of the actuator is divided between its contraction phase and its recovery phase¹⁸. The contraction phase, for the purposes of this research, is considered to be the portion of the cycle in which the rate of change of the volume beneath the bell is negative. At the same time, the recovery phase is considered to be during the cycle when the rate of change of the volume of the bell is positive.

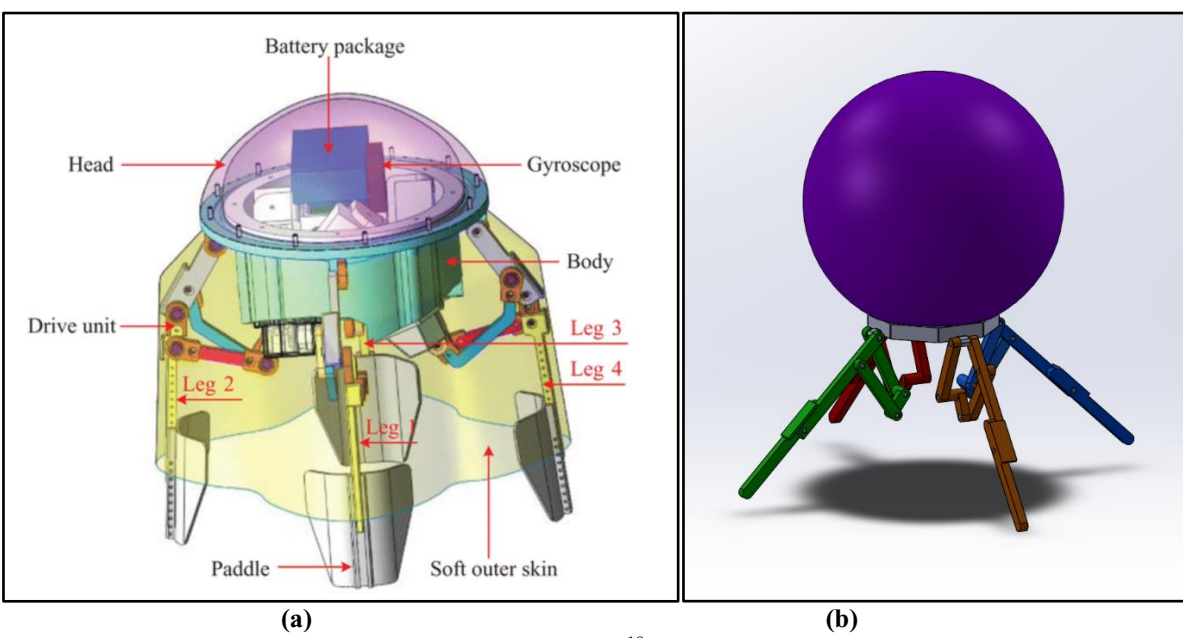


Figure 1. Diagram of (a) Self-propelled Jellyfish-like robot 18 (b) design concept of Jellyfish-Inspired Robot

The volume of flow ejected during the contraction phase is dependent on the length of the link attached to the bell, or lead link or leg, and the change in angle of said link. This paper examines how modifications made to the bell actuator mechanism, primarily based on the extension of the lead link, affect the propulsion force generated by the contraction of the bell. However, the average displacement of the robot is also partially dependent on the volume of water displaced opposite to the forward momentum of the robot during the recovery phase; the difference in the fluid volume displacement between the contraction and recovery

phases determines the net forward thrust produced by the robot. The volume displaced in both phases by each actuator mechanism was calculated to determine which design most efficiently produced forward thrust. These results are presented in Table 2.

Four actuator mechanisms were examined in this paper: a standard four-bara standard six-bar, a modified four-bar, and a modified six-bar. The modifications made to the four- and six-bar are meant to extend the length of the leading link, increasing the total volume within the bell of the robot and ejecting a greater volume of flow during the contraction phase. These modifications are designed to retract during the recovery phase, shortening the effective length of the leading arm to produce less resistance. Figures 2 and 4 demonstrate the movement of the four-bar and six-bar actuators, respectively, while assembled with the body of the robot concept. Figures 3 and 5 demonstrate the modified four- and six-bar actuators, respectively.

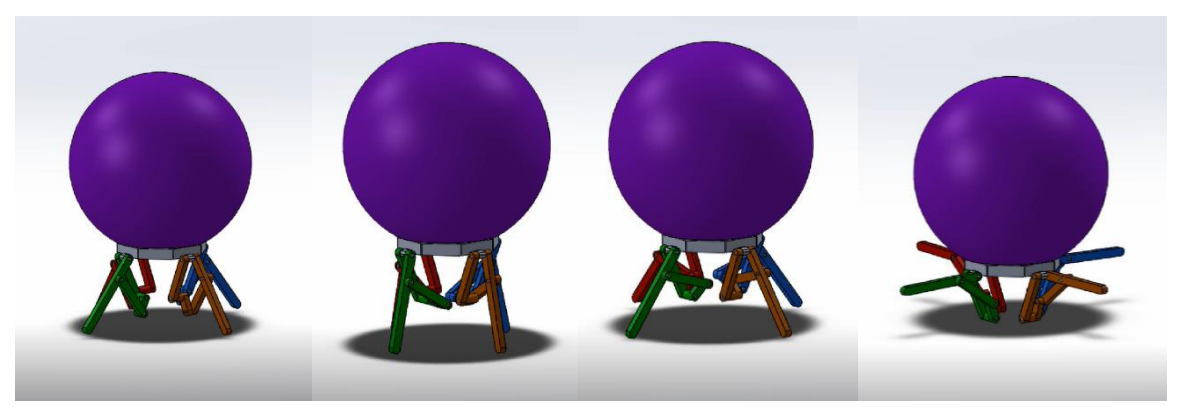


Figure 2. Progression of standard four-bar actuator.

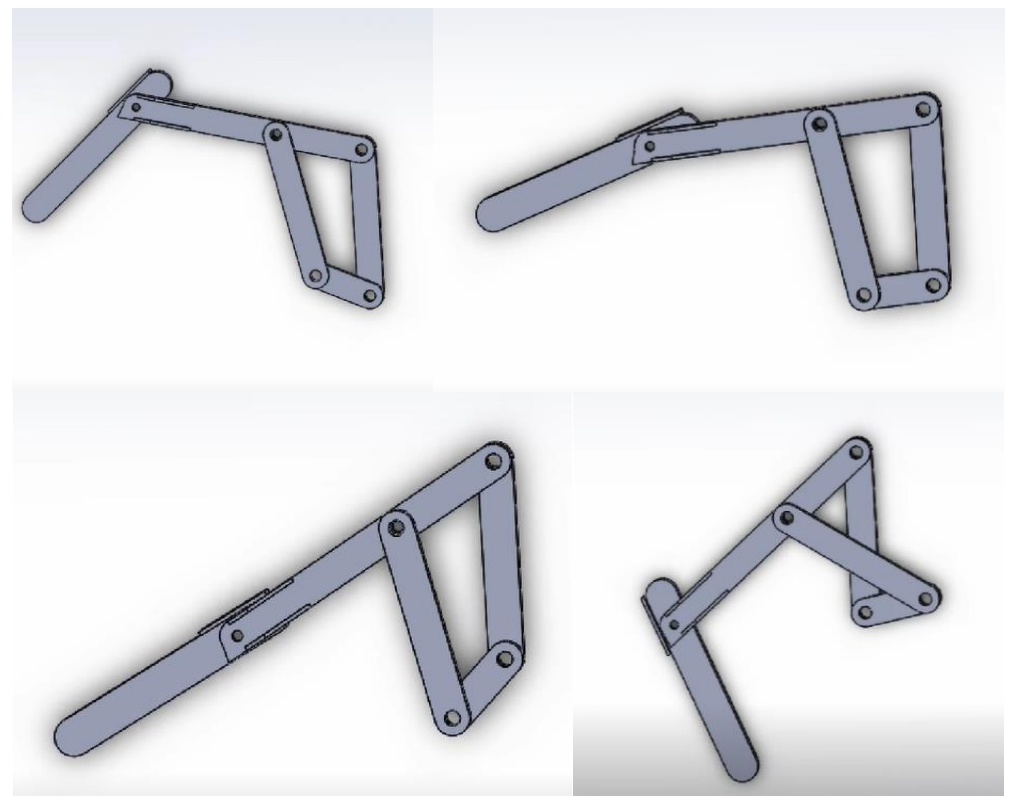


Figure 3 Progression of the extended four-bar actuator (right to left, top to bottom).

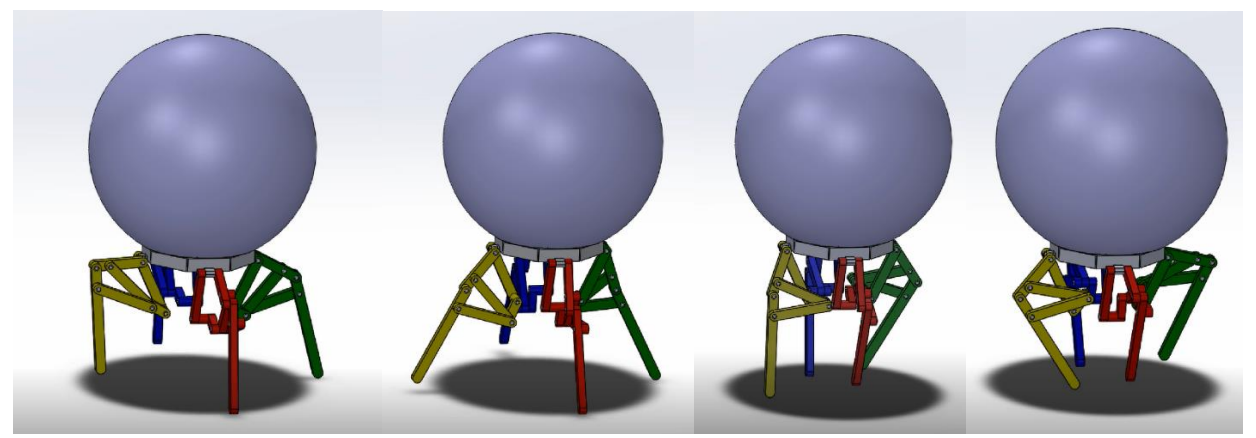


Figure 4. Progression of the standard six-bar actuator.

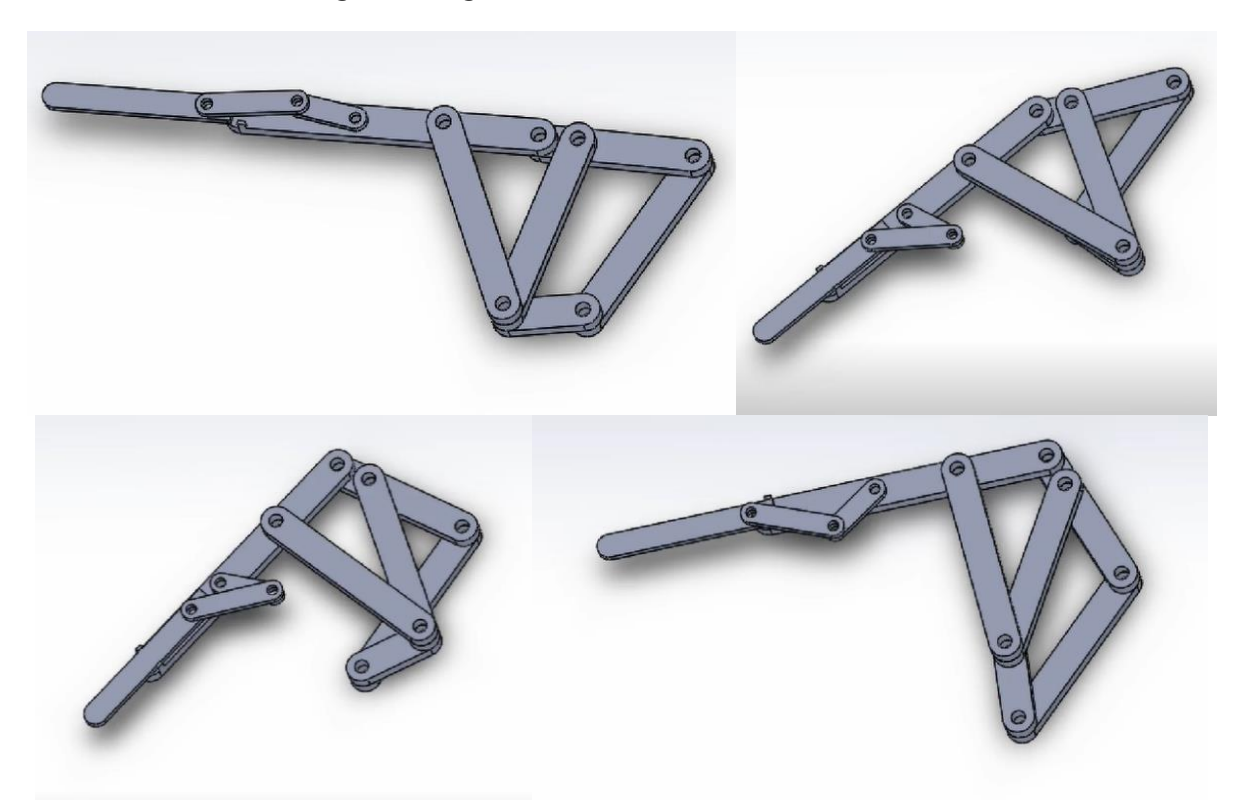


Figure 5. Progression of the extended six-bar actuator (right to left, top to bottom).

B. Dynamic Analysis

The kinematic analyses of the components of each bell actuator design were performed using MechAnalyzer software and MATLAB. Models of the 4 and 6-Bar standard linkages were made using MechAnalyzer, as shown in Figure 6. The lengths of each link used in both models are provided in Table 1; the lengths for the links in the 4-Bar model correlate directly to the lengths of the corresponding links in the standard 4-bar mechanisms shown previously in Figures 2 and 4, while the link lengths for the 6-bar model were scaled down by a factor of 3 in comparison to the 6-bar mechanism shown in Figure 3 and 5. The lead links are specified as L6 and L4 for the 6 and 4-bar mechanisms, respectively. The joints of interest are specified as J2 and J4 for the 6 and 4-bar mechanisms, respectively.

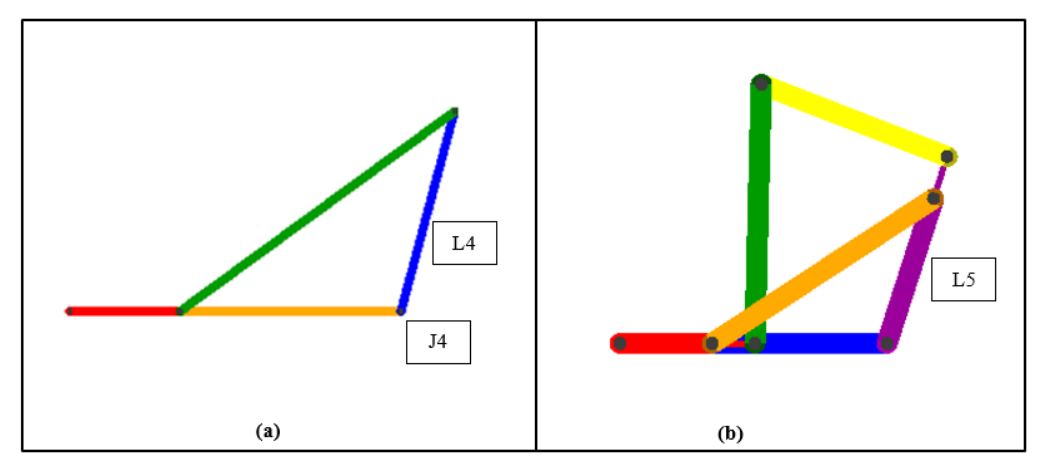


Figure 6. Diagrams of (a) 4-bar linkage and (b) 6-bar linkage.

Table 1. Link lengths of 4 and 6-bar mechanism models.

4-bar mechanism	6-bar mechanism
600 mm	200 mm
200 mm	101 mm
600 mm	200 mm
350 mm	200 mm
	150 mm
	151 mm
	600 mm 200 mm 600 mm

The positional analysis of the L4 link and the J4 joint provided by the MechAnalyzer simulation provides the data for the force analysis for both the standard and extended 4-bar mechanisms. Figure 7 presents the change in angle of Joint 4 and the vertical and horizontal displacement of Link 4 over the duration of one cycle.

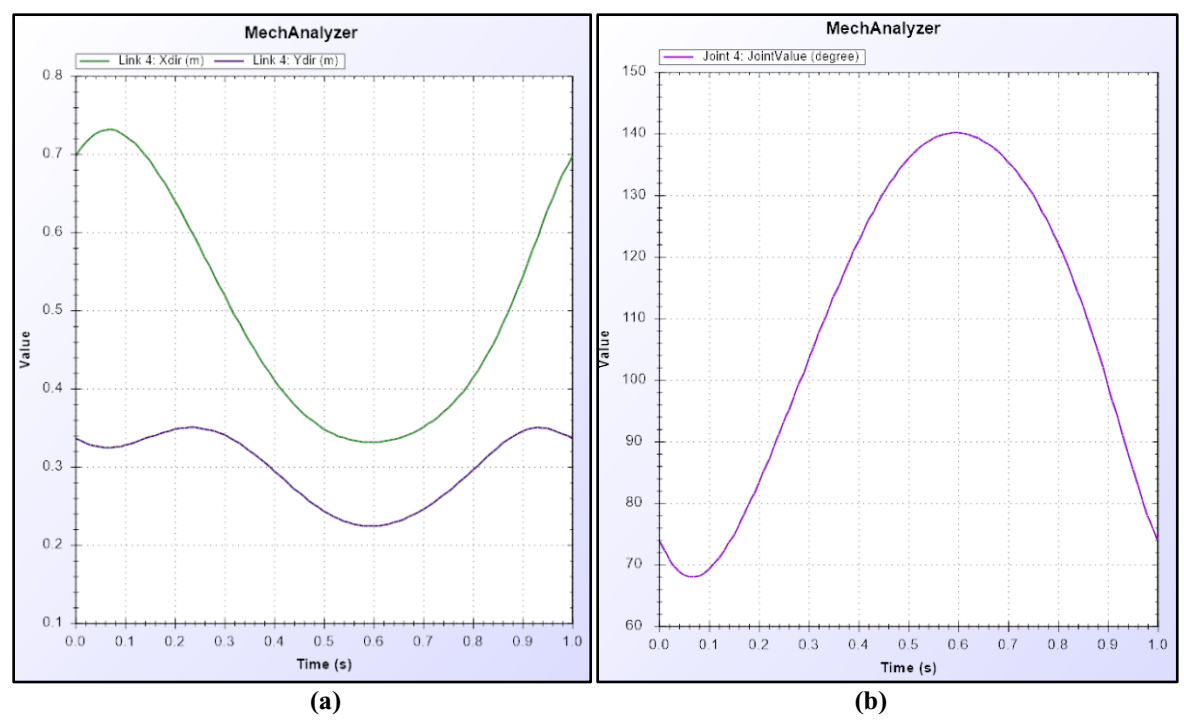


Figure 7. Displacements of (a) link 4 and (b) joint 4 of 4-bar mechanism over time.

The positional data of link 6 and joint 2 of the 6-bar model are shown in Figure 8. The positional data for link 5 was not available in MechAnalyzer, so it was iteratively calculated using the angle of joint 2 and the length of link 5. The lengths of links 5 and 6 were tripled for the purposes of the force calculations in order to better approximate the force generation of the six-bar actuator models.

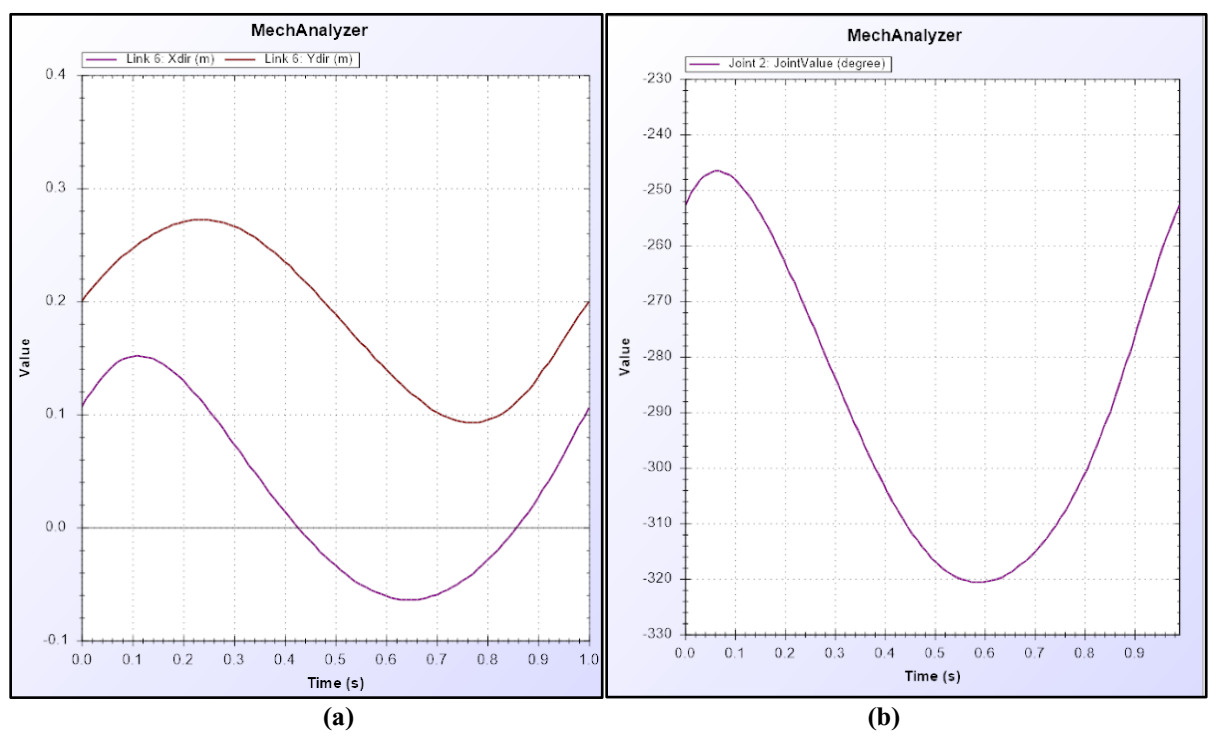


Figure 8. Displacements of (a) link 6 and (b) joint 4 of 4-bar mechanism over time.

C. Force Analysis

The force productions in both the contraction and recovery phases were calculated by deriving the total change in volume underneath the bell from the lengths of the lead links and the change in angles in the joints of interest over a single cycle. The results of the force production calculations indicate that a four-bar actuator provides both the greatest force production and the greatest forward-to-reverse thrust ratio. The equations and calculations for these force production values are provided in the accompanying MATLAB script.

Table 2. Force Production of each actuator mechanism in Contraction and Recovery Phases

Linkage assembly	Lead link(s) length [mm]	Force production (contraction) [10e-5 N]	Lead link(s) length(mm)	Force production [recovery] [10e-5 N]
4-Bar, Standard	L4 = 350	6.87	L4 = 350	.0078
4-Bar, Extended	L4 = 350	6.87	L4 = 150	3.59e-4
6-Bar, Standard	L6 = 450, L5 = 453	0.2235	L6 = 450, L5 = 453	0.2422
6-Bar, Extended	L6 = 550, L5 = 453	0.5384	L6 = 450, L5 = 453	0.2422

III. Fluid Dynamics Analysis of Oscillation of a Sphere

A. Background

Changing the cross-section of an object is an interesting phenomenon, which can be seen in some birds flying in high altitudes as well as in aquatics like squids and jellyfishes. The effect of the deformation for a simple geometry (a circle) when it deforms into an ellipse and returns into its original shape is discussed in

this paper. The physics of this simulation is an interaction between a fluid flow and a solid structure while the structure deforms continuously where the fluid constantly moves along the y-direction. This interaction can be formalized by COMSOL Multiphysics. Therefore, the main purpose of this simulation is to find how deformation in the cross-section area affects the drag, pressure, and viscosity forces, where naturally the birds always do because of the high ratio of respirations in high altitudes. This research is meant to complement the balloon design of the jellyfish-inspired robot and provide insight as to how the oscillation of the balloon's cross-section may impact the motion of the robot in the upper atmosphere.

The model is shown in Figure 9. The fluid flow is considered laminar (Re<2300). The reason for this choice is that the simulation of a turbulent flow causes some wakes and shedding vortexes which may make it very difficult in order to understand what sort of vortexes are because of the turbulent flow or the deformation. Young modulus is considered a typical hyper-elastic material (such as a rubber E=0.1 MPa). The reason is that the hyperelastic materials can tolerate the high strain expansions. The inlet is considered as a vent blowing the air in the y-direction with a constant velocity U=3 cm/s. The other boundaries are determined as the free boundaries where the gradient of the pressure is zero. The top and the bottom of the circle move sinusoidally in opposite directions to each other, providing the deformation of a circle into an ellipse with a constant frequency. The time for the calculation is always considered as four times more than one period of the frequency actuating the top and the bottom of the circle; therefore, the final average results can avoid the initial fluctuations happening when the simulation begins. In addition, the time interval is 0.001 of the time of calculation for the maximum accuracy.

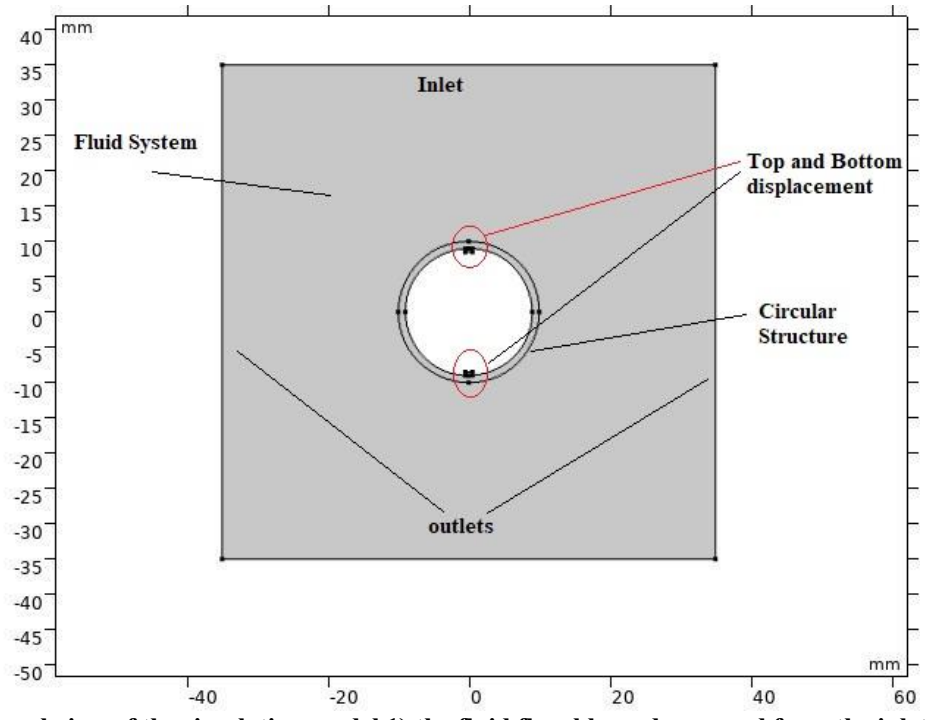


Figure 9. A general view of the simulation model 1) the fluid flow blows downward from the inlet. This means the circular structure moves upward 2) The top and bottom parts of the circular structure move in the opposite direction to each other $U = U_0 sin(\omega t)$ where ω is the frequency of the deformation.

The drag, pressure, and viscosity forces on the circle boundaries are calculated during the deformation process. Because the simulation is time-dependent, the results are in a range of numbers showing the forces in each time interval. In addition, the mesh network consists of triangular elements where the maximum dimensions cannot exceed 0.5 mm.

The general governing equations for fluid-structure interaction in a 2D polar coordinate system is:

$$m^2 \frac{\partial^2 U}{\partial t^2} + K. \nabla^4 U + \Delta p = 0 \tag{1}$$

$$\frac{\partial p}{\partial t} + \frac{\partial \rho u}{\partial r} + \frac{\rho \partial u}{\partial r} = 0 \tag{2}$$

$$\frac{\partial u}{\partial t} + \frac{u\partial u}{\partial r} + \frac{c^2}{\rho} \frac{\partial \rho}{\partial r} = 0 \tag{3}$$

where U is the velocity of the structure, p is pressure, p is density, u is the velocity of the fluid flow, and c is the sound speed in the fluid system. Eq. (1) is the structural dynamic mechanical equation and Eqs. (2) and (3) are the fluid dynamic equations for a compressible fluid flow. Liu et al. 9 show that if the main diameter of the circle changes harmonically, the velocity can be a harmonic function. Because the top and the bottom parts of the circular structure moves sinusoidally, we can conclude that the velocity of the fluid upon the structure is a harmonic function, which means:

$$\frac{\partial^2 u}{\partial t^2} = -\omega^2 u \tag{4}$$

where ω is the deformation frequency. This assumption can transform the governing equations as the first and second Bessel functions.

$$u = A.I(s) + B.Y(s) \tag{5}$$

where J(s) and Y(s) are the first and second Bessel functions, respectively. A and B are the function of time, where can be calculated based on the boundary conditions. The main idea of this project is not an analytical solution for the deformation; however, the analytical solution can give a better view of the mathematical nature of the deformation in a fluid-structure system.

B. Results

Figure 10 shows the deformation of the circular structure during the simulation process. The three forms of the circle, vertical and the horizontal ellipse, continuously transform to each other when displacement deformation moves sinusoidally over time. Table 3 shows the forces acting on the circular structure when it has each shape without change in time.

Table 3. comparison of three forces for each shape. All dimensions are N/m

	Vertical Ellipse	Circle	Horizontal Ellipse	Average
Drag Force	-9.2e-6	-1e-5	-1.3e-5	-1.1e-5
Pressure Force	-4.8e-6	-6e-6	-9e-6	-6.6e-6
Viscosity Force	-4.4e-6	-4e-6	-3e-6	-3.8e-6

The average drag force has a minus sign because it acts in the opposite direction (downward) during the simulation where the structure has an upward movement.

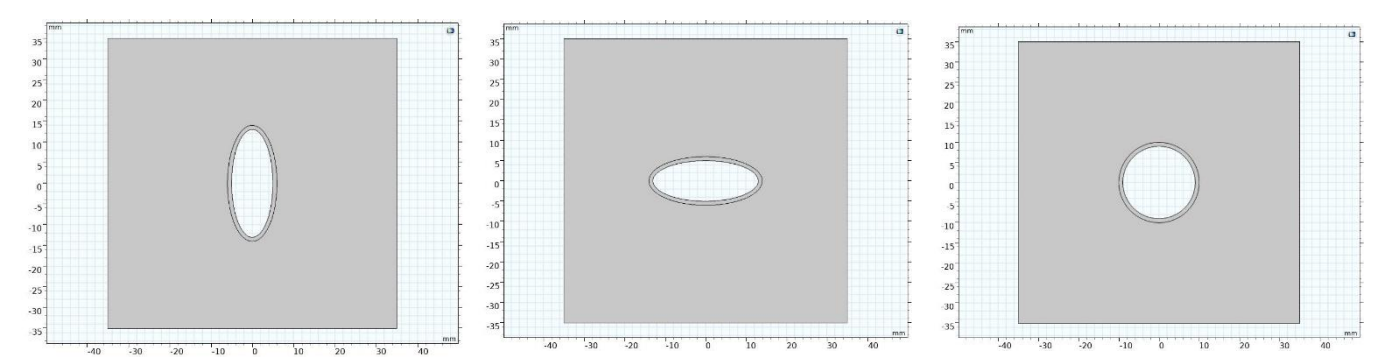


Figure 10. The transformation of the circular structure into a circle, horizontal and vertical ellipse during the simulation.

When the circular structure deforms continuously during the simulation, all the three shapes transform into each other with the same frequency of displacement. Figure 11 shows the three forces acting on the deforming structure changing by time. The sinusoidal function is expected because the function should be harmonic due to Eq. (4). The time of the calculation is four times the period of the deforming process. Each time interval is at least 0.01 of each period; therefore, the software output consists of values of each force in each time interval (which is at least 400 values). If the average of each force is calculated, the final data can be listed in Table 4.

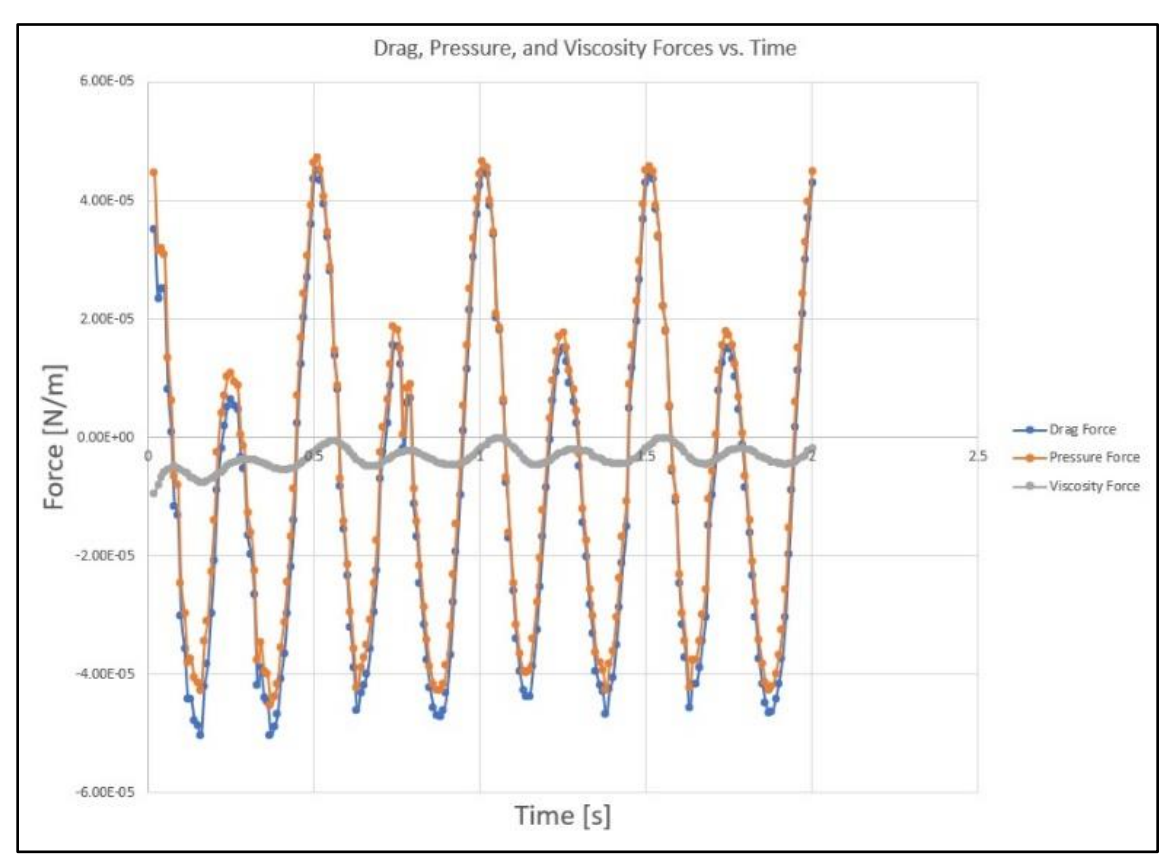


Figure 11. Change of drag, pressure, and viscosity forces during the time when the frequency is 2 Hz, and the magnitude of the displacement is 2 mm.

Table 4. The average of the three forces in different frequencies when the magnitude of the displacement is 4 mm. The critical frequency is highlighted.

Force	0.125 Hz	0.25 Hz	0.5 Hz	1 Hz	2 Hz	4 Hz	5 Hz	8 Hz	10 Hz
Drag	-8.6e-6	-8.7e-6	-8.7e-6	-8.7 e-6	-7.8e-6	-2.7e-6	-3.6e-6	6.89e-6	1.89e-5
Pressure	-5.6e-6	-5.7e-6	-5.7e-6	-5.7e-6	-4.9e-6	1.66e-7	-6e-6	9.82e-6	2.2e-5
Viscosity	-3e-6	-3e-6	3e-6	3e-6	3e-6	2.9e-6	3e-6	2.8e-6	3e-6

As a conclusion from Table 4, the average of the drag forces in a deforming structure is less than the average of the forces in every three different shapes. This means that the vortexes that happen during the deformation significantly change the drag, pressure forces. The viscosity forces are the same because the viscosity of the air is negligible. The vortex and the pressure distribution of the deforming circular structure are shown in Figure 12. The distributions of vortexes in each pattern of the deforming structure are different from the ones happening in each shape individually. Moreover, the distribution of the pressure also is shown in Figure 13.

Table 4 also shows that a drop happens in a critical frequency (2 Hz), which means that in the lower frequency, nothing changes in all the forces. However, the drop in the drag force happens in this frequency, and the decrease in the force continues so that it changes into the trust force (with a positive sign). This means in higher frequencies, even the deformation of the shape can induce a force that helps the structure moves along the flight direction. The value of the critical frequency depends on the magnitude of the deformation vibration. Table 5 shows that the critical frequency increases when the magnitude of the displacement decreases. This means the Reynolds number changes when the displacement magnitude changes, and it seems to be the reason for the change in the critical frequency. Moreover, the vortexes in higher frequencies are different compared to the ones in the lower frequencies. Figure 12 compares these vortexes and shows the differences.

Table 5. The critical frequency is dependent on the magnitude of the displacement.

The magnitude of displacement	4 mm	2 mm	1 mm
Critical Frequency	2 Hz	4 Hz	10 Hz

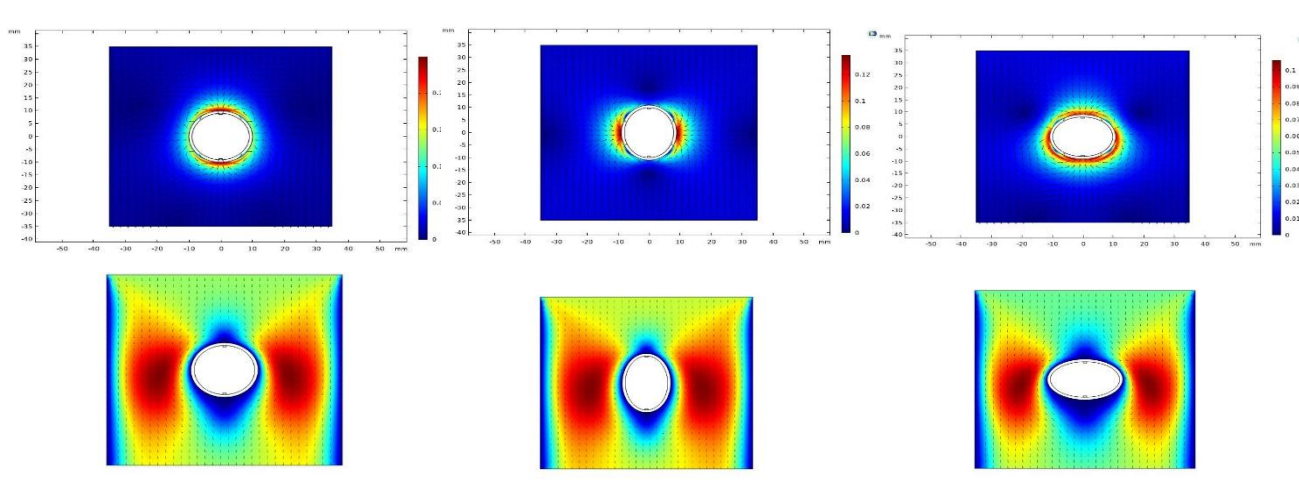


Figure 12. The velocity vortexes in two cases: when the circular structure deforms (the top pictures) and when each shape without any deformation (the bottom pictures)

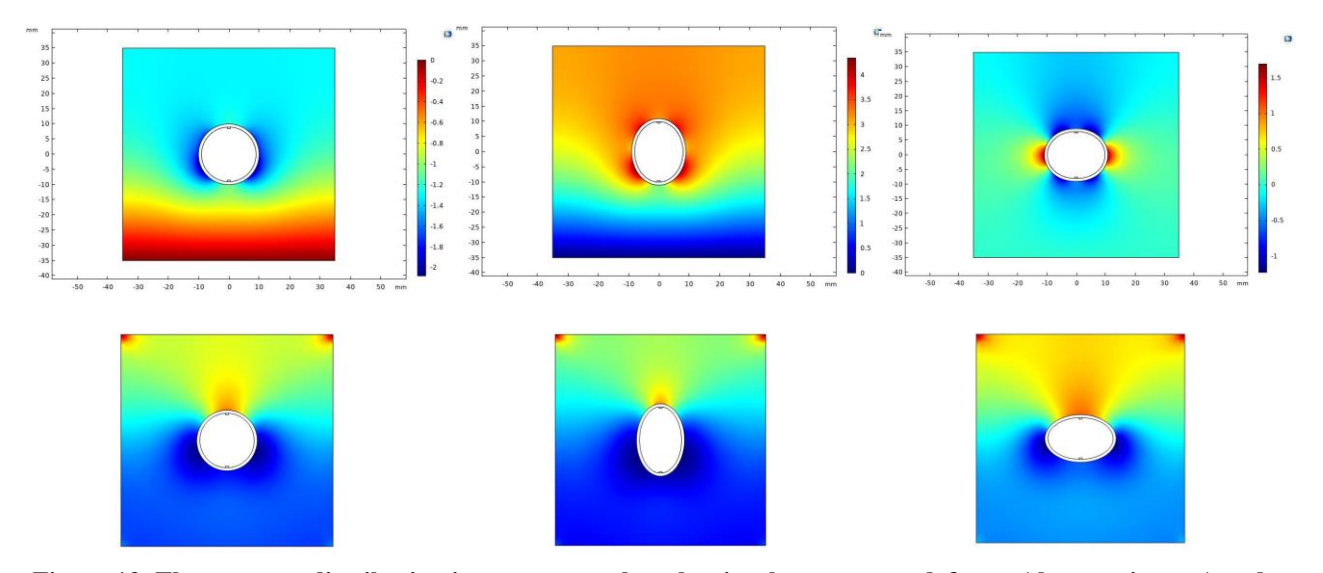


Figure 13. The pressure distribution in two cases: when the circular structure deforms (the top pictures) and when each shape without any deformation (the bottom pictures).

IV. Design of the Flagellate Robot

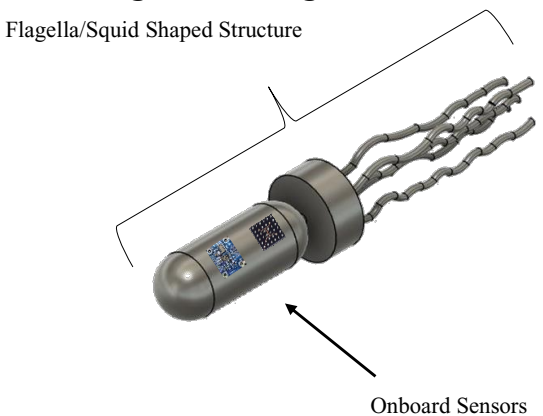


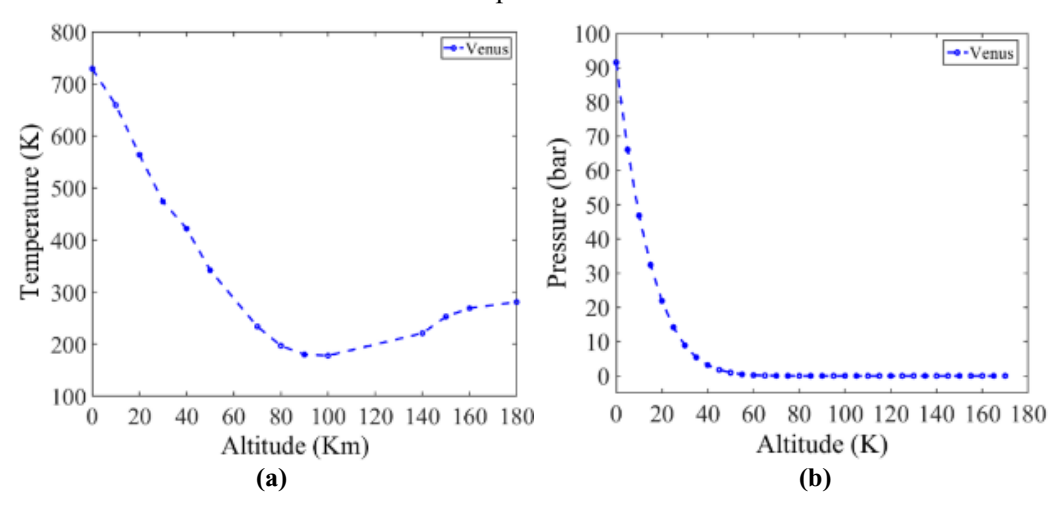
Figure 14. Flagella Micro-Robot Concept for Venus Upper Atmosphere Exploration.

A. The Climate of Venus

Venus has a similar mass, density, chemical composition, and gravity compared to Earth's. However, as discussed, it also has un-friendly qualities like hot temperature extremes, acidic-like atmosphere, and crushing pressures (about 92 times that of Earth's)^{1,2}. Its atmosphere is almost entirely composed of Carbon Dioxide and is much denser than Earth, composed of opaque clouds of sulfuric acid. The upper atmosphere of Venus exhibits a super-rotation effect where the atmosphere circles the planet in just 4 Earth days. High wind speeds in higher elevations support this super-rotation phenomenon.

Due to these harsh conditions, information about the planet's topography has been made through radar imaging. Venus' characteristics make it extremely challenging in designing surface and atmospheric exploration systems intended to have long-duration missions. However, at around a range between 50 to 65 km above the surface of the planet, the atmospheric pressure and temperature are comparatively the same as that of Earth's. In fact, Venus' upper atmosphere is marked as the most Earth-like atmosphere in the Solar System and is the designated location for exploration and colonization.

Average temperature, pressure, and wind speed profiles for Venus are shown in Fig. 15. Observe that within the 50 to 65 km range, wind speeds are at a maximum, reaching up to about 96 m/s. That is a significant amount of energy that can be stored and harvested from a low-power, lightweight system that will have months to year-long mission durations. In addition, within this altitude range, standard electronics would be able to operate. Commercial/standard electronics have an operational range between 32°F to 158°F. Thus, the operation of a small system within this range can be equipped with various sensors and equipment needed to conduct various scientific experiments.



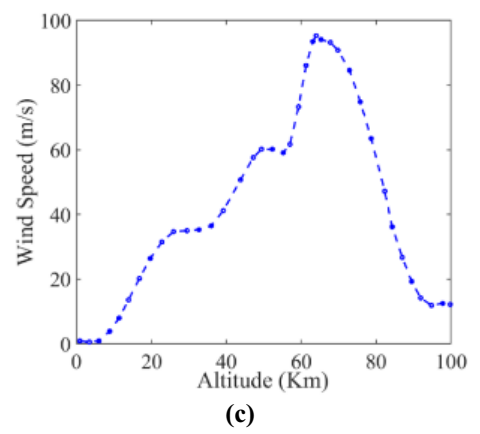


Figure 15. Views of (a) temperature, (b) pressure, and (c) wind speed profiles as a function of altitude for Venus¹⁻³.

B. Wind Harvesting on Venus

The upper atmosphere of Venus rotates at an incredible velocity, forcing winds to accumulate to up to about 345 kilometers per hour. Conversely, at the surface, there is almost little to no wind or just a gentle breeze. In 2020, NASA ran a public challenge to develop an obstacle avoidance sensor for a potential Venus rover, the AREE. While previous landers lasted from minutes to a couple of hours, AREE would be powered for long-duration surface missions utilizing a wind-turbine mechanism that harnesses the available Venusian winds to provide power for scientific instruments and mobility.

Wind energy harvesting can be achieved by considering wind power principles from fluid mechanics. In the case of a wind turbine, power generation can be highly effective during high-velocity winds. NASA has performed tests of wind turbines in Antarctica stations where there are extreme temperatures. According to Betz' Law, the theoretical maximum power produced from a wind turbine is about 60%. The amount of power (P) that can be extracted from a turbine depends on the turbine efficiency (η), atmospheric density (ρ [kg/m³]), swept area of the turbine (A [m²]), and the wind speed (ν [m/s]), modeled by Eq. (6)²0. $P = \frac{1}{2} \dot{m} v^2 = \frac{1}{2} \eta \rho A v^3$ (6)

The scope of this work focuses on the development of a singular device that harnesses the available atmospheric winds, which can provide reliable, year-round power on Venus.

C. Flagellates/Squid-like Hybrid System

Bacteria Flagellum is a thin, hair-like structure that acts like an actuator in the cells of organisms. There are many types of flagella, but both prokaryotic and eukaryotic flagella are primarily used for "swimming" locomotion, providing a whip-like, propulsive movement. This mobility is similar to that found in the flying squid. The flying squid uses a jet propulsion motion by taking water into its siphon muscle from one side and pushing it out the other side. They have been observed to reach distances up to 30m above the ocean surface.

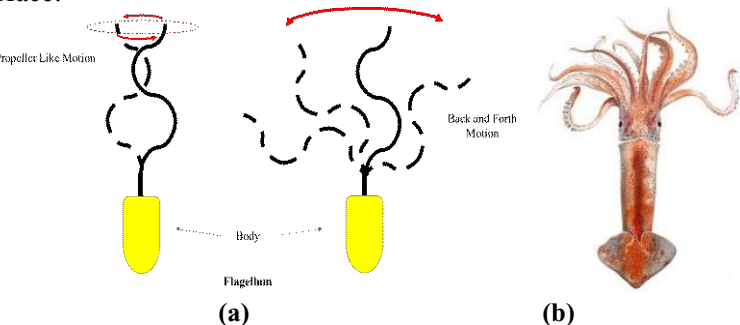


Figure 14. (a) Bacterium flagella and (b) flying squid.

Studies have tried to replicate this method of locomotion from both organisms to produce aquaticaerial vehicles²⁰. Considering Venus' dense atmosphere, it would be a scientific breakthrough to develop an aerial system that harnesses this propulsion power while simultaneously using the available winds for power. This concept enables a whole new perspective of aerospace missions and provides a great leap in capabilities for the aerospace and aviation industries. These bacteria-like structures can "swim" through the upper atmosphere of Venus, undertaking future aerospace missions, expanding the region covered by traditional rovers, landers, and orbiters, recording a variety of sensory measurements such as air temperature, ground-penetrating radar, pressure, climate conditions, etc.

C. Flagellates Prototyping

Some progress has been made in prototyping the flagellate and jellyfish robots. Several tail configurations (Fig. 15), and molds for said tails, were designed using SOLIDWORKS. Both were 3D printed using PLA. Once the molds were complete, smooth on 00-30 silicone was poured inside. The silicone was set for around 4 hours, and the tails were complete. The internal circuits of the flagellates used a nano Arduino, a 7.4V LiPo battery, a 3.0V DC motor, a button, and a few other electrical components. Testing the robots involved sealing them in a water-filled tank. The larger jellyfish robot was made from a 3D printed PLA base and motor housings fixed to a 24-inch beach balloon. Carbon fiber rods acted as the linkage system to translate motion from the motor to the lead links (Fig. 15). The main body was filled with helium to aid in movement. The internal circuit used a mega Arduino, a breadboard, L293D motor drivers, eight double shaft 3.0V DC motors, two 7.4V LiPo batteries, and a few other electrical components.



Figure 14. (a) Straight tail, off-centered, (b) Helical tail, and (c) Straight tail, centered.

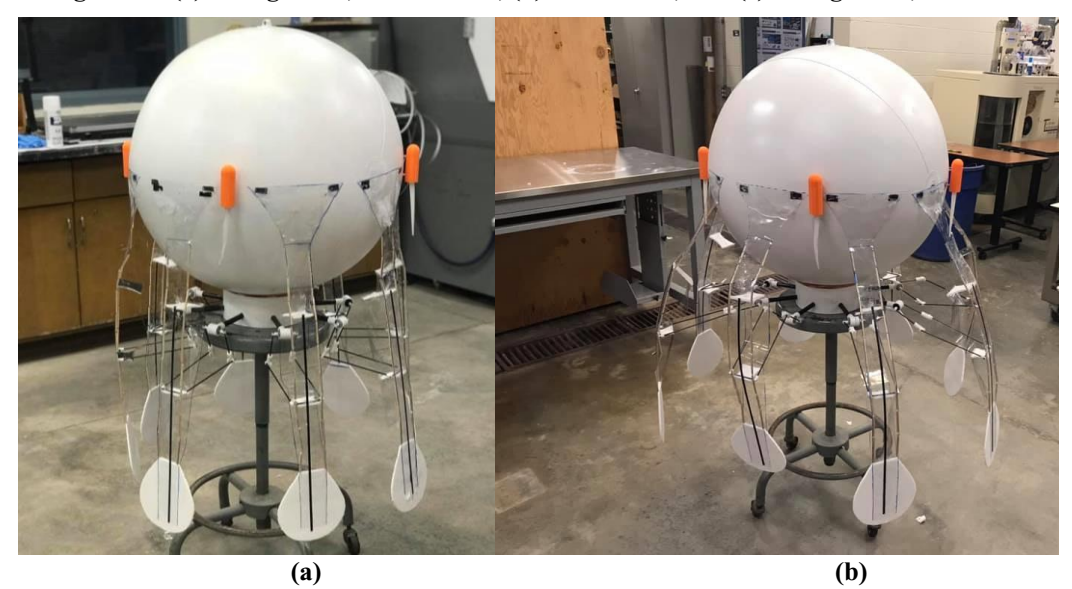


Figure 15. Initial prototype of jellyfish carrier robot with legs (a) relaxed and (b) extended.

The flagellates would then be turned on via the button on their circuit, and observed to see if they sank/swam and the pattern in which they do so. To test the larger jellyfish robot, the main "body" would be filled with helium gas, and the motors turned on. The helium-filled body and the moving legs were designed to allow it to float and be able to move around. Although the research was conceptual, getting a prototype for robots that can be propelled forwards is a step in the right direction. What was primarily shown was the ease of manufacturing and the relatively simplistic design of these small, flagellated robots and the larger jellyfish robot. There are more tail configurations to be tested, and making the body more compact is also desired. Future testing would focus on optimizing the tail shape and motion for "swimming" and adding sensor hardware, as well as analyzing and improving the mobility of the jellyfish prototype.

V. Conclusion

This article builds on a previous design for a jellyfish-inspired swimming robot to propose and compare four- and six-bar actuation mechanisms for the purpose of jet propulsion of robot through a fluid, as well as propose further modifications to adapt the design for upper atmospheric exploration on Venus. CAD models for four different actuation mechanisms were built and animated to demonstrate their motion. The linkage mechanisms were modeled using MechAnalyzer, and the motion of the relevant joints and linkages were recorded and used to calculate the change in volume of the bell of the robot in both a contraction and recovery phase. Force analysis of the mechanisms suggests that four-bar mechanisms produce more thrust and have a higher forward-to-reverse thrust ratio over the duration of a single cycle. Future research will refine the force calculation and kinematic models as well as propose design optimization methods to achieve the highest forward-to-reverse thrust ratio. Simulation of a simple deformation in a circle was performed in this paper. Drag, pressure, and the viscosity forces acting on a circular hyper-elastic structure are calculated by COMSOL Multiphysics. The average of the forces resulted from the simulation compared to the average forces acting on each circle, vertical and horizontal ellipse without any deformation by time. The results showed that the deformation during the movement by time could significantly reduce the drag and pressure forces; thus, the act of high ratio respiration of the birds in high altitudes can help them during their flying. Moreover, the effect of the vibrational magnitude on the critical frequency when the drag force drops shows that it happens in a higher frequency when the magnitude is lower. This article also discussed a complimentary flagellate robot that would collect data during exploration missions. The conceptual design, inspiration, and sensors were discussed, and prototyping methods and tests were explained.

I. Acknowledgements

The authors Emily Strauss, and Mostafa Hassanalian gratefully acknowledge the financial support from the National Science Foundation. This study was supported by the INTENSE REU program. The INTENSE REU is funded by the National Science Foundation (NSF) Division of Engineering Education and Centers (EEC) award #1757793. The project is led at New Mexico Tech by PI Dr. Michael Hargather and Co-PI Dr. Mostafa Hassanalian.

References

¹Acosta, G., and Hassanalian, M., "Power minimization of fixed-wing drones for Venus exploration in various altitudes," *Acta Astronautica*, Vol. 180, pp. 1-15, 2021.

²Acosta, G.A., Grow, D. and Hassanalian, M., "Design and Analysis of a High Pressure and High Temperature Fixed Wing Space Drone for Venus Exploration", 2019 AIAA Aviation Forum, Dallas, TX, 17-21 June 2019.

³Rubin, Z., Aboelezz, A., Herkenhoff, B., Hassanalian, M., "Drones for Venus Exploration: Energy Harvesting Mechanisms and Thermal-based Flight Control," 2021 AIAA SciTech Forum, Virtual Event, 11–15 & 19–21 January 2021.

⁴Hassanalian, M., Rice, D., Johnstone, S., Abdelkefi, A., "Performance analysis of fixed wing space drones in different solar system bodies," *Acta Astronautica*, Vol. 152, pp.27-48, 2018.

⁵Hassanalian, M., Rice, D., Abdelkefi, A., "Evolution of space drones for planetary exploration: a review," *Progress in Aerospace Sciences*, Vol. 97, pp. 61-105, 2018.

⁶Hassanalian, M., Rice, D., Johnstone, S., Abdelkefi, A., "Planetary exploration by space drones: design and challenges", 2018 AIAA Aviation Conference, Atlanta, Georgia, 25-29 June 2018.

⁷Howell E., "NASA asks public to design sensors for Venus rover concept," *SPACE.com*, [online database], 19 Mar. 2020, URL: https://www.space.com/nasa-venus-rover-challenge-aree.html.

⁸Sherman, M., Hassanalian, M., "Microrobots Inspired by Oceanic and Bacteria Organisms for Observations of Venus' Upper Atmosphere," 18th VEXAG Meeting 2020, Virtual Event, 16-17 November 2020.

⁹Gammill, M., Hassanalian, M., "Manta Ray Inspired Drone for Venus Exploration: Biological-Solution for Extreme Conditions," 18th VEXAG Meeting 2020, Virtual Event, 16-17 November 2020.

¹⁰Herkenhoff, B., Fisher, J., Hassanalian, M., "Performance Analysis of Solar Fixed-wing Drones on Venus," 18th VEXAG Meeting 2020, Virtual Event, 16-17 November 2020.

¹¹Hassanalian, M., Mohammadi, S., Acosta, G., Guido, N., Bakhtiyarov, S., "Surface temperature effects of solar panels of fixed-wing drones on drag reduction and energy consumption," *Meccanica*, pp.1-20, 2020.

¹²Hassanalian, M., Pellerito, V., Sedaghat, A., Sabri, F., Borvayeh, L. and Sadeghi, S., "Aerodynamics loads variations of wings with novel heating of top surface: bioinspiration and experimental study," *Experimental Thermal and Fluid Science*, Vol. 109, p.109884, 2019.

¹³Hassanalian, M., Ben Ayed, S., Ali, M, Houde, P., Hocut, C., Abdelkefi, A., "Insights on the wing colorization of migrating birds on their skin friction drag and the choice of their flight route," *Journal of Thermal Biology*, Vol. 72, pp. 81-93, 2018.

¹⁴Herkenhoff, B., Fisher, J., Dinelli, C., Hassanalian, M., "Energy Harvesting Techniques for Hybrid Amphibious Drones in the Marine Environment", 2020 AIAA Propulsion and Energy Conference, Virtual, 24-26 August 2020.

¹⁵Gammill, M., Hassanalian, M., "Power Analysis of Fixed-Wing UAVs for Titan Exploration in Various Altitudes", 2020 AIAA Propulsion and Energy Conference, Virtual, 24-26 August 2020.

¹⁶Olivas, M., Gammill, M., Hassanalian, M., "Conceptual Design of Fueling Mechanism for an Unmanned Aerial Vehicle with Harvesting Liquid-Methane Capability on Titan", 2020 AIAA Aviation Forum, Virtual, 15-19 June 2020.

¹⁷Yu, J., Xiao, J., Li, X. and Wang, W., "Towards a miniature self-propelled jellyfish-like swimming robot," *International Journal of Advanced Robotic Systems*, Vol. 13, No. 5, p.1729881416666796, 2016.

¹⁸Ren, Z., Hu, W., Dong, X. and Sitti, M., "Multi-functional soft-bodied jellyfish-like swimming," *Nature communications*, Vol. 10, No. 1, pp.1-12. 2019.

¹⁹Liu, P., Tang, B.J. and Kaewunruen, S., V"ibration-induced pressures on a cylindrical structure surface in compressible fluid," *Applied Sciences*, Vol. 9, No. 7, p.1403, 2019.

²⁰Hou, T., Yang, X., Su, H., Jiang, B., Chen, L., Wang, T. and Liang, J., "Design and experiments of a squid-like aquatic-aerial vehicle with soft morphing fins and arms," In 2019 International Conference on Robotics and Automation (ICRA) (pp. 4681-4687), IEEE, May 2019